Monthly Notices
of the
ROYAL ASTRONOMICAL SOCIETY

MNRAS **494,** 363–377 (2020)
Advance Access publication 2020 March 18

doi:10.1093/mnras/staa748

Detection of neutral atomic species in the ultra-hot Jupiter WASP-121b

Samuel H. C. Cabot [1]★ Nikku Madhusudhan [2] Luis Welbanks,[2] Anjali Piette [2] and Siddharth Gandhi [3]

[1]*Department of Astronomy, Yale University, 52 Hillhouse, New Haven, CT 06511, USA*
[2]*Institute of Astronomy, Madingley Road, Cambridge CB3 0HA, UK*
[3]*Department of Physics, University of Warwick, Coventry CV4 7AL, UK*

Accepted 2020 March 7. Received 2020 March 2; in original form 2019 November 18

ABSTRACT

The class of ultra-hot Jupiters comprises giant exoplanets undergoing intense irradiation from their host stars. They have proved to be a particularly interesting population for their orbital and atmospheric properties. One such planet, WASP-121b, is in a highly misaligned orbit close to its Roche limit, and its atmosphere exhibits a thermal inversion. These properties make WASP-121b an interesting target for additional atmospheric characterization. In this paper, we present analyses of archival high-resolution optical spectra obtained during transits of WASP-121b. We model the Rossiter-McLaughlin effect and the Centre-to-Limb Variation and find that they do not significantly affect the transmission spectrum in this case. However, we discuss scenarios where these effects warrant more careful treatment by modelling the WASP-121 system and varying its properties. We report a new detection of atmospheric absorption from H α in the planet with a transit depth of 1.87 ± 0.11 per cent. We further confirm a previous detection of the Na I doublet, and report a new detection of Fe I via cross-correlation with a model template. We attribute the H α absorption to an extended Hydrogen atmosphere, potentially undergoing escape, and the Fe I to equilibrium chemistry at the planetary photosphere. These detections help to constrain the composition and chemical processes in the atmosphere of WASP-121b.

Key words: planets and satellites: atmospheres.

1 INTRODUCTION

Ultra-hot Jupiters (UHJs) display some of the most extreme physics of all known exoplanets. These massive gas giants have close-in, often tidally locked orbits with their host stars, and are subject to extremely strong irradiation. UHJs offer fascinating case studies in their own right: they have equilibrium temperatures in excess of 2000 K (Fortney et al. 2008; Parmentier et al. 2018), can contain vaporized metals in their atmospheres (Casasayas-Barris et al. 2018; Hoeijmakers et al. 2018), and often have orbits completely misaligned from their host star's rotation (Triaud et al. 2010; Anderson et al. 2018). Some orbit close to their Roche limit, and are on the verge of tidal disruption (Delrez et al. 2016). Others have extended, escaping atmospheres (Yan & Henning 2018). These unusual properties test and inform theories of how hot Jupiters form and evolve, and improve our understanding of their atmospheric chemistry and dynamics.

An outstanding problem is how these planets attain their close-in orbits. An *in-situ* scenario is often thought unlikely since proximity to the host star is not conducive for gas giant formation, though recent studies have shown that rapid accretion of hot gas may be possible (Batygin, Bodenheimer & Laughlin 2016). The other scenario is migration, either through the protoplanetary disc, or via dynamical scattering with other bodies (Dawson & Johnson 2018). Chemical tracers such as relative amounts of C and O help constrain whether formation occurs within or beyond the snow line (Öberg, Murray-Clay & Bergin 2011; Madhusudhan, Amin & Kennedy 2014b). Present day orbital obliquities favour dynamical scattering (Triaud et al. 2010), as does the fact that most semimajor axes are lower bounded by twice the Roche limit ($a/a_R \sim 2$) (Ford & Rasio 2006). However, several hot Jupiters in orbits of $a/a_R < 2$ require alternative or more complex histories, such as tidal decay (see Delrez et al. 2016; Dawson & Johnson 2018, for more detailed discussions). A comprehensive understanding of the dynamics and chemistry of hot Jupiters is thus imperative to resolve these issues.

With transit spectroscopy, UHJs are some of the easiest planets to characterize. High temperatures give UHJs relatively high day-side flux contrasts with respect to their host stars, and their large radii (usually 1–2 R_J) yield strong transit depths. To date, several UHJs have been studied through transmission and emission spectroscopy. Some examples include KELT-9b (Hoeijmakers et al. 2018), MASCARA-2b (Casasayas-Barris et al. 2019), WASP-121b (Evans et al. 2017), WASP-33b (Nugroho et al. 2017),

★ E-mail: sam.cabot@yale.edu

Table 1. Exposure information for each night of observation. Rows correspond to (1) observing start time; (2) observing end time; (3) min. and max. exposure durations; (4) approximate signal-to-noise of wavelength bins along the continuum; (5) number of in-transit exposures to number of total exposures; (6) airmass evolution throughout the night; (7) WASP-121b orbital phase coverage (mid-transit at $\phi = 0$ and 1).

Night	2017-12-31	2018-01-09	2018-01-14
$T_{\rm start}$ (UTC)	01:39	00:34	01:18
$T_{\rm end}$ (UTC)	08:16	08:38	08:43
$t_{\rm exp}$ (s)	570–720	500–600	500–660
$\rm SNR_{cont}$	∼36	∼25	∼31
$N_{\rm in\text{-}transit}/N_{\rm total}$	13/35	18/55	18/50
sec z	1.339 → 1.015 → 1.329	1.501 → 1.015 → 1.626	1.225 → 1.015 → 1.826
ϕ	0.883 → 0.099	0.907 → 0.170	0.853 → 0.095

WASP-103b (Cartier et al. 2017), and WASP-18b (Sheppard et al. 2017; Arcangeli et al. 2018; Espinoza et al. 2019). A number of neutral and ionized atomic species have been predicted in the atmospheres of such UHJs (Kitzmann et al. 2018; Lothringer, Barman & Koskinen 2018). In particular, phase-resolved high-resolution transmission spectroscopy has proved an excellent way to probe hot Jupiter atmospheres. The cross-correlation approach (Snellen et al. 2010) involves comparing observed spectra with a model template of a species in order to detect forests of weak absorption lines. Molecular, atomic, and ionized species have been detected this way (Snellen et al. 2010; Birkby 2018; Alonso-Floriano et al. 2019; Hoeijmakers et al. 2019). Strong features, such as the Na doublet and Balmer lines can be directly recovered by co-adding multiple in-transit spectra (Wyttenbach et al. 2015; Casasayas-Barris et al. 2019). With sufficient phase-coverage, it is possible to resolve day-to-night side winds (Louden & Wheatley 2015) and extended or escaping atmospheres (Ehrenreich et al. 2015).

One planet of particular interest is the ultra-hot Jupiter WASP-121b ($T_{\rm eq} = 2358 \pm 52$ K), which is in a near-polar orbit around a bright ($V = 10.44$) F-type star (Delrez et al. 2016). It's semimajor axis is only ∼1.15 times its Roche limit, suggesting the planet is on the verge of tidal disruption. Deformation models suggest the planet may have radius $R_{\rm sub} \sim 2R_{\rm jup}$ at its sub-stellar point (Delrez et al. 2016). The bright host star and extended atmosphere makes the planet a prime target for characterization. Indeed, the planet has been studied extensively. Evans et al. (2016) detected H_2O in the atmosphere of WASP-121b using a transmission spectrum obtained using *the Hubble Space Telescope* (*HST*) WFC3 spectrograph and ground-based observations. Evans et al. (2017) reported a detection of H_2O and a thermal inversion in the dayside atmosphere using a thermal emission spectrum obtained with *HST* WFC3. However, a direct detection of TiO or VO proved elusive in subsequent transit and secondary eclipse studies (Evans et al. 2018; Mikal-Evans et al. 2019). Recent optical phase curves from *TESS* along with other data confirm the presence of a thermal inversion in the dayside atmosphere (Bourrier et al. 2019; Daylan et al. 2019). While species such as H-, TiO, and VO have been suggested as possible inversion-causing absorbers in the planet (Bourrier et al. 2019; Daylan et al. 2019), a variety of other absorbers may also be responsible (Mollière et al. 2015; Gandhi & Madhusudhan 2019). Separately, Salz et al. (2019) suggested excess broad-band NUV absorption might be due to Fe II, a species later detected by Sing et al. (2019), in addition to Mg II. The ionized gas extends out to $R_p/R_s \sim 0.3$, and might be undergoing atmospheric escape or be confined due to a magnetic field.

WASP-121b currently lacks a comprehensive transit study at high-resolution in the optical regime. Here, we analyse three transits of WASP-121b observed by HARPS. While Sindel (2018) detect the Na doublet in transmission using one order of this data set, we present additional detections of the H α line and Fe I by analysing the full wavelength coverage. Our paper is organized as follows. In Sections 2 and 3 we present the data set, preprocessing steps, and review methodology of phase-resolved high-resolution transmission spectroscopy. We present atomic detections in Section 4, and discuss their implications for the atmosphere of WASP-121b in Section 5. Additionally in Section 5, we investigate the impact of the Rossiter-McLaughlin effect and Centre-to-Limb Variation on the transmission spectra.

2 OBSERVATIONS

Our data set consists of archival optical spectra of WASP-121 acquired by the HARPS (High-Accuracy Radial-velocity Planet Searcher) echelle spectrograph, located at the ESO La Silla 3.6 m telescope. At a resolution of ∼115 000, HARPS coverage spans 380–690 nm over 68 spectral orders. The raw data were reduced with the HARPS Data Reduction Software (DRS) v3.8, which performs blaze correction and Th-Ar wavelength calibration, and produces 1D spectra rebinned on to a uniform 0.01 Å barycentric rest-frame wavelength grid. Observations were conducted over the nights of 2017 December 31, 2018 January 9, and 2018 January 14 (hereafter Nights 1, 2, and 3) as part of the Hot Exoplanet Atmospheres Resolved with Transit Spectroscopy program (HEARTS) Program 0100.C-0750(C) (PI: D. Ehrenreich). There are 140 exposures in total, with 49 acquired during the transit (Table 1).

Absorption due to H_2O and O_2 in Earth's atmosphere produces strong telluric features at wavelengths upwards of ∼500 nm. We use the ESO tool `molecfit` v1.5.7, which fits a line-by-line radiative transfer model (LBLRTM) of Earth's transmission spectrum to observed telluric features (Smette et al. 2015). Whereas some previous works construct an empirical telluric model (Wyttenbach et al. 2015; Casasayas-Barris et al. 2018), we opt to use `molecfit` for the much lower S/N exposures analysed here. However, care must be taken to avoid fitting to stellar absorption lines (Allart et al. 2017; Casasayas-Barris et al. 2019; Hoeijmakers et al. 2019). For each exposure, on each night, we shift the DRS wavelength solution to the telescope rest-frame using the Barycentric Earth Radial Velocity (BERV). We identify regions suitable for telluric fitting by: (1) obtaining centroids of ∼300 of the strongest known telluric features in a model telluric spectrum obtained from `molecfit` (Smette et al. 2015; Allart et al. 2017); (2) obtaining a $T_{\rm eff} = 6500$ K `phoenix` stellar model (Husser et al. 2013); (3) Doppler shifting the model to the same radial velocity as WASP-121 (the

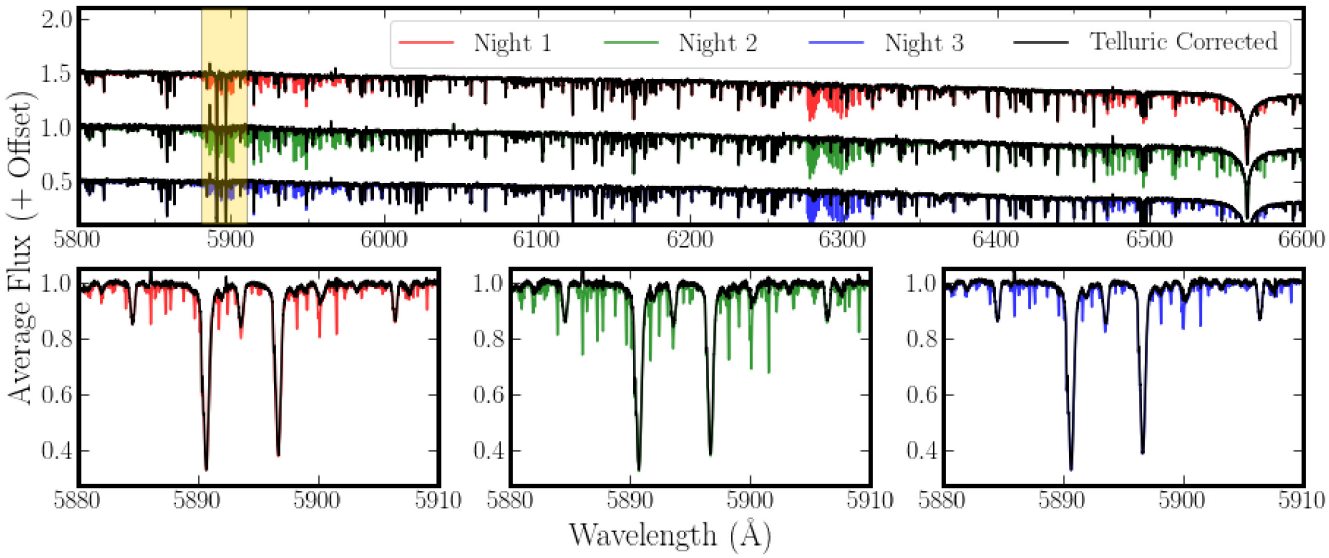

Figure 1. Telluric correction with `molecfit`. *Top panel*: Co-added and normalized spectra for Nights 1, 2, and 3 are depicted in colour (red, green, and blue, respectively). The black curves are the co-added spectra after dividing out the telluric model. The yellow stripe denotes the zoom-in wavelength range. *Bottom panels*: same as above, but cropped in a narrow wavelength range around the Sodium Doublet, for each night. Water vapour is the predominant telluric absorber in this range.

sum of the systemic velocity and BERV); (4) choosing tellurics preselected in step (1) whose locations fall outside of features in the stellar model; and (5) selecting small wavelength ranges centred on these telluric features. We provide `molecfit` location and ambient weather parameters from the HARPS DRS output, and fit parameters similar to those used by Allart et al. (2017). After fitting, we use the included `calctrans` tool to calculate a high-resolution model telluric spectrum over the full wavelength range. We finally divide the observed spectrum by the model (Fig. 1). There is slight overcorrection at 5885 Å, possibly from an extra water feature in the line-data base; however it is offset sufficiently as to not influence the planetary Na absorption. There is no apparent telluric sodium emission, which we verified by inspecting simultaneous sky spectra from fibre B.

3 METHODS

In this section, we discuss our extraction of the planetary transmission spectrum using the technique of Wyttenbach et al. (2015). We treat each night separately throughout the analysis, and propagate the Poisson-uncertainties of the data. We also discuss our cross-correlation procedure, based on Snellen et al. (2010), which lends itself to detecting species with a multitude of weak features.

3.1 Transmission spectra

During a transit event, an exoplanet blocks part of its host star along our line of sight and causes the star to appear dimmer. The change in brightness is approximately the ratio of the area occulted by the planet to the area of the stellar disc,

$$\Delta_0^2 = \left(\frac{R_p}{R_*}\right)^2. \tag{1}$$

This wavelength-integrated quantity is often referred to as the white-light transit depth. Beyond the grey photospheric radius, the planet's atmosphere absorbs additional light at specific wavelengths, which produces its transmission spectrum. The amount of absorption at a given wavelength depends on the abundance and cross-section of the absorbing species.

Given an atmospheric height $H(\lambda)$, we denote the wavelength-dependent transit depth as:

$$\begin{aligned}\Delta_\lambda^2 &= \left(\frac{R_p + H(\lambda)}{R_*}\right)^2 \\ &= \left(\frac{R_p}{R_*}\right)^2 + \left(\frac{H(\lambda)}{R_*}\right)^2 + \frac{2R_p H(\lambda)}{R_*^2} \\ &\simeq \Delta_0^2 + \frac{2R_p H(\lambda)}{R_*^2},\end{aligned} \tag{2}$$

where we assume $H(\lambda) << R_*$ (an atmosphere generally extends 5–10 scale heights, or several thousand kilometres for a hot-Jupiter) (Madhusudhan et al. 2014a). Using the ephemeris of Delrez et al. (2016) (Table 2), we identify 13, 18, and 18 in-transit exposures for Nights 1, 2, and 3, respectively. We denote in-transit and out-of-transit spectra as $f(\lambda, t_{\rm in})$, and $f(\lambda, t_{\rm out})$. Each night's time-series covers the entire ∼2.5 h transit, plus several hours of baseline exposures before and after the transit.

Several effects can affect the fidelity of the transmission spectrum. These include: telluric absorption by species in Earth's atmosphere; the reflex motion of the host star induced by the planet's orbit; the Rossiter-Mclaughlin (RM) effect; Centre-to-Limb Variation (CLV); and the planet's changing radial velocity throughout the transit. All of these are resolved at the HARPS spectral resolution (Louden & Wheatley 2015; Wyttenbach et al. 2015; Allart et al. 2017; Yan et al. 2017; Casasayas-Barris et al. 2019). We systematically address each of these effects. Having corrected for tellurics with `molecfit`, we linearly interpolate all spectra on to a common wavelength grid, and Doppler shift each to correct for the stellar reflex velocity:

$$v_{\rm reflex} = -K_* \sin 2\pi\phi. \tag{3}$$

Note, there is no apparent Interstellar Medium (ISM) Sodium absorption. Otherwise, the reflex velocity correction could prevent

Table 2. Literature values for stellar, orbital, and planetary parameters for WASP-121b and its host star.

Parameter	Symbol	Unit	Value
Star			
V-magnitude	m_V	mag.	10.4
Effective temperature	$T_{\rm eff}$	K	$6460\ ^{+140}_{-140}$
Proj. rot. velocity	$v\sin i$	km s^{-1}	$13.56\ ^{+0.69}_{-0.68}$
Stellar mass	M$_\star$	$M_\odot$	$1.353\ ^{+0.080}_{-0.079}$
Stellar radius	R$_\star$	$R_\odot$	$1.458\ ^{+0.030}_{-0.030}$
Stellar semi-amplitude	K_*	km s^{-1}	$181\ ^{+6.3}_{-6.4}$
System			
Mid-transit time	T_0	HJD$_{\rm TDB}$	$2456635.70832\ ^{+0.00011}_{-0.00010}$
Transit duration	τ	d	$0.1203\ ^{+0.0003}_{-0.0003}$
Period	P	d	$1.2749255\ ^{+0.00000020}_{-0.00000025}$
Semimajor axis	a	A.U.	$0.02544\ ^{+0.00049}_{-0.00050}$
Limb-darkening coefficient	$u_{1,r'}$	–	$0.290\ ^{+0.014}_{-0.014}$
Limb-darkening coefficient	$u_{2,r'}$	–	$0.305\ ^{+0.325}_{-0.007}$
Systemic velocity	γ	km s^{-1}	$38.350\ ^{+0.021}_{-0.021}$
Planet			
Orbital inclination	i_p	deg.	$87.6\ ^{+0.6}_{-0.6}$
Sky proj. obliquity	β	deg.	$257.8\ ^{+5.3}_{-5.5}$
Equilibrium temperature	$T_{\rm eq}$	K	$2358\ ^{+52}_{-52}$
Planetary mass	M$_p$	M$_{\rm J}$	$1.183\ ^{+0.064}_{-0.062}$
Planetary radius*	R$_p$	R$_{\rm J}$	$1.865\ ^{+0.044}_{-0.044}$
Planetary semi-amplitude**	K_p	km s^{-1}	$217\ ^{+19}_{-19}$

Notes: All values from Delrez et al. (2016).
*corrected for asphericity.
**calculated from $M_p/M_* = K_*/K_p$.

its cancellation when we later divide in-transit and out-of-transit spectra (Casasayas-Barris et al. 2018). Following a thorough investigation (Section 5.2), we find CLV and RM induced effects lie at the noise level of the data, and we neglect their correction. Since WASP-121b is in a near-polar orbit ($\beta \sim 257.8°$), it obscures regions of similar velocity throughout the transit. As such, the RM distortion of stellar absorption lines blurs out when stacked in the planet rest-frame. Also, WASP-121 is a hot, F6V-type star, and the CLV effect on the transmission spectrum is expected to be negligible (Yan et al. 2017).

We create a master out-of-transit spectrum by co-adding individual out-of-transit spectra:

$$\hat{f}_{\rm out}(\lambda) = \sum_{t_{\rm out}} f(\lambda, t_{\rm out}) \tag{4}$$

and compute individual transmission spectra as:

$$\Re(\lambda, t_{\rm in}) = \frac{f(\lambda, t_{\rm in})}{\hat{f}_{\rm out}(\lambda)}. \tag{5}$$

The continuum level of each spectrum it is affected by throughput variations from the instrument and weather. Therefore we normalize each $\Re(\lambda, t_{\rm in})$ by fitting and dividing by a fifth-order polynomial. The planet's apparent radial velocity is given by,

$$v_{\rm pl} = K_p \sin 2\pi\phi + \gamma, \tag{6}$$

where K_p is the semi-amplitude and γ is the systemic velocity (Table 2). Throughout the transit, $v_{\rm pl}$ changes by $\sim$100 km s^{-1}, corresponding to a Doppler shift of 2 Å, or 200 pixels. To avoid smearing out the atmospheric signal, we Doppler shift each $\Re(\lambda, t_{\rm in})$ by $-v_{\rm pl}(t_{\rm in})$ and stack them in the rest-frame of the planet:

$$\hat{\Re}(\lambda) = \sum_{t_{\rm in}} \Re(\lambda, t_{\rm in})|_{v_{\rm pl}(t_{\rm in})}. \tag{7}$$

Finally, we apply a median filter of width 1501 pixels to remove remaining broad-band variations. It is important to precisely define $\hat{\Re}(\lambda)$. Since we have lost continuum information, $\hat{\Re}(\lambda)$ corresponds to the transmission spectrum of the planet, after removing the white-light transit depth $\Delta_0^2 = (R_p/R_*)^2$. Values less than unity correspond to absorption by the planet's atmosphere. For further analysis, we define the quantity:

$$\delta(\lambda) \equiv -\hat{\Re}(\lambda) + 1 = \Delta_\lambda^2 - \Delta_0^2 \simeq \frac{2R_p H(\lambda)}{R_*^2}, \tag{8}$$

where $\delta(\lambda)$ is the *excess* transit depth caused by the atmosphere of the planet. Positive values correspond to atmospheric absorption.

Normalization with a polynomial is common practice in previous literature (e.g. Casasayas-Barris et al. 2018; Seidel et al. 2019), and can be applied before division by the master-out (Allart et al. 2017), after division (Seidel et al. 2019), or after stacking individual transmission spectra (Casasayas-Barris et al. 2018). Typically it is done with a third or fourth degree polynomial; we found a fifth degree suitable for the large wavelength range in our analysis. Finally, we stack the co-added transmission spectra from each night to obtain a master transmission spectrum (Fig. 2).

3.2 Cross-correlation

Strong features such as the Na doublet, H Balmer lines, the Ca II triplet, the Mg I triplet, and He I have been detected in hot gas giants by directly extracting their transmission spectra (Wyttenbach et al. 2015; Casasayas-Barris et al. 2018; Nortmann et al. 2018; Cauley et al. 2019). However, atomic and molecular species can produce a dense forest of thousands of weak absorption lines (Gandhi et al. 2019; Hoeijmakers et al. 2019). We can search for these species by cross-correlating with a model transmission spectrum, which stacks the signal from all of the absorption lines. This approach has been used successfully in the optical regime (Nugroho et al. 2017; Hoeijmakers et al. 2018, 2019), as well as the near-infrared (Snellen et al. 2010; Brogi et al. 2012; Birkby et al. 2013; Rodler, Kürster & Barnes 2013; Lockwood et al. 2014; Piskorz et al. 2016; Birkby et al. 2017; Brogi et al. 2018; Hawker et al. 2018). We use the `x-cor` pipeline, which was previously used to detect CO, H_2O, and HCN in the dayside atmospheres of hot Jupiters (Hawker et al. 2018; Cabot et al. 2019). In the near-infrared, strong telluric absorption warrants aggressive preprocessing, often through use of Principal-Component-Analysis (PCA) or its uncertainty weighted version (SYSREM) (Tamuz, Mazeh & Zucker 2005). In the optical regime, the `molecfit` model is sufficient for telluric correction. We apply a sliding filter to each spectrum which flags $\geq 5\sigma$ outliers and replaces them with the median value in the window. We mask the chip gap and 1 per cent of data from either end of the full spectrum which suffer from low throughput or strong telluric contamination. Following from the previous section, all residuals are currently in the planetary rest-frame. Finally, we remove any remaining broad-band variations by applying a 75-pixel width high-pass filter, and subtracting the mean of each wavelength bin.

Cross-correlation involves a model template, which is derived from a theoretical transmission spectrum of one or multiple species. Model spectra generation is discussed in the following section. To obtain the template, we subtract the maximum value in a 0.008 Å-sliding window across the model spectrum to remove its continuum.

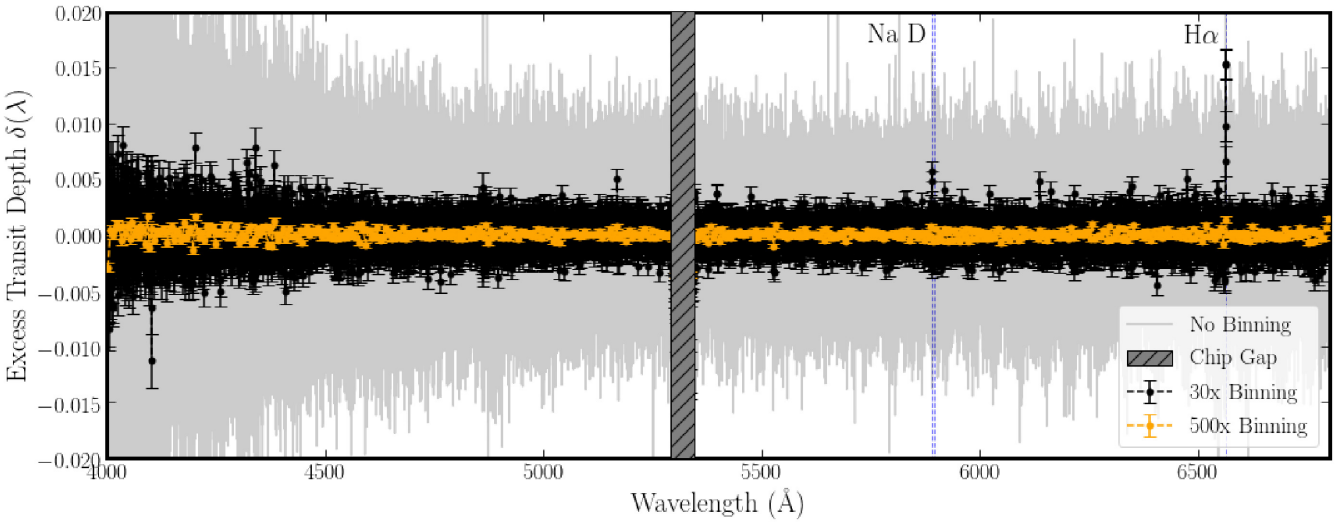

Figure 2. Excess transit depth from the atmosphere of WASP-121b, over the full analysed wavelength range. Particularly notable are the Sodium D-lines and Hα feature; although a few other features visibly extend from the continuum. We show the unbinned data, and data binned by 30× and 500× pixels. The HARPS chip gap is masked in our analysis.

The template is convolved with a narrow Gaussian filter of full width at half-maximum (FWHM) = 0.8 km s^{-1} to match approximately the wavelength sampling of the HARPS detector (Hoeijmakers et al. 2019), and subsequently normalized to unity. We define our cross-correlation-function (CCF) as a function of velocity and time:

$$\mathrm{CCF}(v,t) = \frac{\sum_i m_i|_v w_i x_i(t)}{\sum_i m_i|_v w_i}, \tag{9}$$

where m_i is our model template Doppler shifted by v, $x_i(t)$ is the observed transmission spectrum over wavelength bins i, and w_i are weights assigned to each bin. Weights are the time-axis variance of each wavelength bin, which effectively down-weights noisy pixels that are affected by low throughput, or lie in the cores of telluric or stellar lines (Brogi et al. 2016). The normalization term in equation (9) preserves the intrinsic strength of the absorption features. That is, the CCF returns a weighted average of line-depths in the data (Hoeijmakers et al. 2019). We perform cross-correlation over a velocity grid spanning $-600 \leq v \leq 600$ km s^{-1} in steps of 2.0 km s^{-1}.

If the model template contains species native to the host star, then this procedure reveals the Doppler Shadow from the Rossiter-McLaughlin effect (Cegla et al. 2016). Indeed, the Doppler Shadow dominates the CCF, and must be removed for atmospheric analysis. We cross-correlate with a $T_{\rm eff}$ = 6500 K `phoenix` stellar template. Then the Doppler Shadow and other broad-band variations are modelled by fitting a third-order polynomial to the in-transit CCF values at each sampled velocity. Our approach differs from that used in a previous study of KELT-9 b (Hoeijmakers et al. 2019), where a time-varying Gaussian profile is iteratively fit to the shadow and atmospheric signal. We attempted this approach but could not obtain robust fits. The WASP-121 RM residual has asymmetric negative wings on its edges, and is not well-approximated by a Gaussian. The CCF RM residual is a reflection of the RM residuals of individual lines, which also have this shape (see Section 5.2). The shape might come from a combination of the weak Centre-to-Limb Variation and normalization step; in-transit stellar lines should be 'missing' the flux occulted by the planet, but these might cause the appearance of excess flux in the wings. We attempted simultaneous fitting of a positive and negative Gaussian profile, but this allowed too many free parameters for the relatively low S/N data (WASP-121 is about three magnitudes fainter than KELT-9, and we have fewer in-transit exposures per night). Our polynomial-fit approach works well in our case because the RM effect spans a small velocity range, whereas the planetary signal is spread over ∼100 km s^{-1}. When cross-correlating with other templates, we scale the Doppler Shadow model to fit the CCF, and subsequently subtract it to isolate the atmospheric signal. The full process is shown in Fig. 3. We excluded Night 2 from cross-correlation analysis due to its low S/N.

Since the planet's radial velocity changes throughout the transit, the absorption signal appears as a moving trail. The planet velocity is uniquely determined by a certain combination of semi-amplitude and systemic velocity (equation 6). We sample these two parameters from a grid, and for each combination, Doppler shift the CCFs by the corresponding planet velocities, and subsequently co-add them. The correct combination stacks the planet signal in-phase, boosting the S/N. Incorrect combinations gives us a noise estimate from which we compute detection significance.

3.3 Model spectra

We model high-resolution spectra for WASP-121b assuming a H_2-He dominated clear atmosphere with gaseous atomic Fe. The model spectra are generated using an adaptation of the AURA model for exoplanetary transmission spectra (e.g. Pinhas et al. 2018). The spectra are computed using line-by-line radiative transfer in a plane-parallel atmosphere in transmission geometry. The model atmosphere is divided in 100 layers uniformly distributed in log space between pressures of 10^2–10^{-6} bar and assumes hydrostatic equilibrium along with a uniform chemical volume mixing ratio of the species of interest. The model sets the planetary radius, uncorrected for asphericity, at a reference pressure of 100 mbar. We adopt an isothermal temperature profile at 2400 K, roughly the equilibrium temperature of the planet assuming full redistribution and zero albedo. The model spectra are calculated using 3×10^5 wavelength points in a uniform wavelength grid from 0.4–0.7 μm, corresponding to a resolution of $R \sim 4$–7×10^5, higher than the

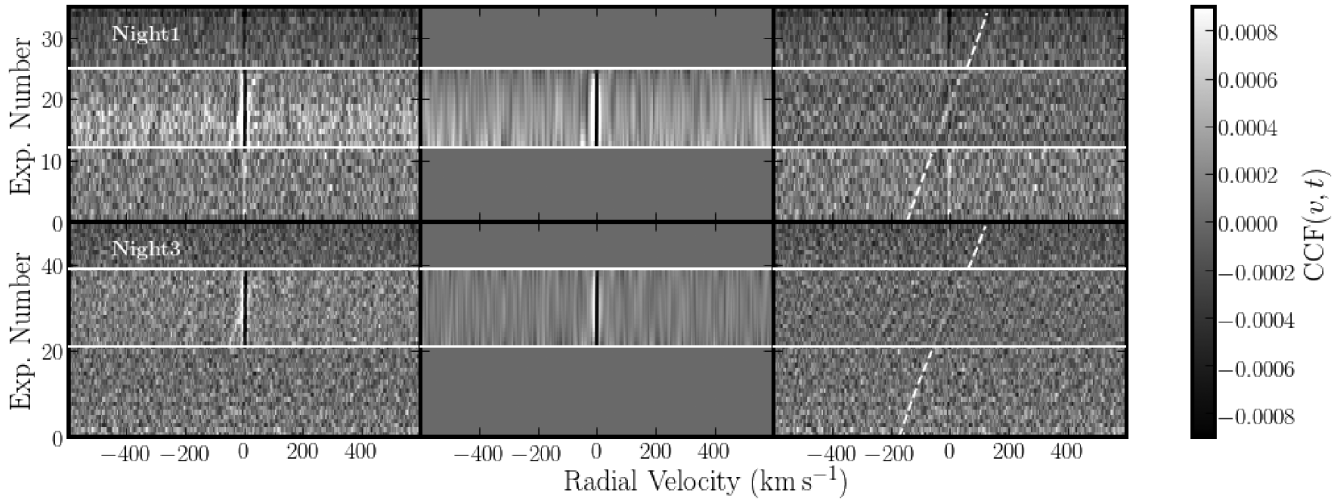

Figure 3. Time-series cross-correlation functions (CCFs) of WASP-121 spectra with a `phoenix` model template. Spectra were Doppler shifted by the known V_{sys} of WASP-121 prior to cross-correlation. Horizontal white lines mark the start and end of transit. Each row shows the procedure for a different night of observation. *First column*: Time-series CCFs. *Second column*: Polynomial fit to each column of the CCFs, which serves as a model of the Doppler Shadow RM residual. *Third column*: CCFs after subtracting the Doppler shadow model. The white dashed lines mark the velocity of WASP-121b before and after transit. A faint white trail in the in-transit frames represents absorption by the atmosphere of WASP-121b through features in common with the `phoenix` model.

resolving power of the instrument. The system parameters (e.g. planetary and stellar radii, planetary gravity, and orbital semimajor axis) are obtained from Delrez et al. (2016) (see Table 2).

Motivated by recent elemental detections in UHJs we search for multiple species in the atmosphere of WASP-121b and empirically detect Fe. Our present model atmosphere considers absorption due to gaseous atomic Fe along with the effects of collision-induced-absorption (CIA) due to H_2–H_2 and H_2–He (Richard et al. 2012) and H_2 Rayleigh scattering. The atomic opacity is calculated following the methods of Gandhi & Madhusudhan (2017) with absorption cross-sections computed from NIST (Kramida et al. 2018). We assume the volume mixing ratio of Fe in the atmosphere to be 10^{-7}, which is a lower limit on the Fe abundance feasible in this atmosphere as discussed below. The volume mixing ratios of H and He are calculated assuming an He/H_2 ratio of 0.17 and requiring the sum of the abundances to be unity.

We verify that neutral atomic Fe is the dominant Fe species using equilibrium chemistry calculations computed with the HSC CHEMISTRY software (version 8) (e.g. Pasek et al. 2005; Bond, Lauretta & O'Brien 2010; Elser, Meyer & Moore 2012; Madhusudhan 2012; Moriarty, Madhusudhan & Fischer 2014; Harrison, Bonsor & Madhusudhan 2018). These calculations assume solar elemental abundances (Asplund et al. 2009) and include the same species as Harrison et al. (2018) plus gaseous, solid, neutral, and ionic molecules and atomic forms of Fe, Ti, V, Cr, and Mg. Fig. 4 shows the equilibrium abundances of several neutral gaseous Fe species between 1000 and 3000 K at a pressure of 1 mbar nominally corresponding to the optical photosphere. At the equilibrium temperature of WASP-121b (∼2400 K), neutral atomic Fe is the dominant form of Fe and should therefore be the most easily detected (also see Kitzmann et al. 2018; Lothringer et al. 2018). We note that the terminator temperature probed in the optical at high resolution, i.e. going as high up in the atmosphere as 1 mbar −1 μbar, can be significantly lower than the equilibrium temperature. As such the Fe abundance can be significantly lower than the maximum Fe abundance possible at high T of $\sim 10^{-5}$, as seen in Fig. 4.

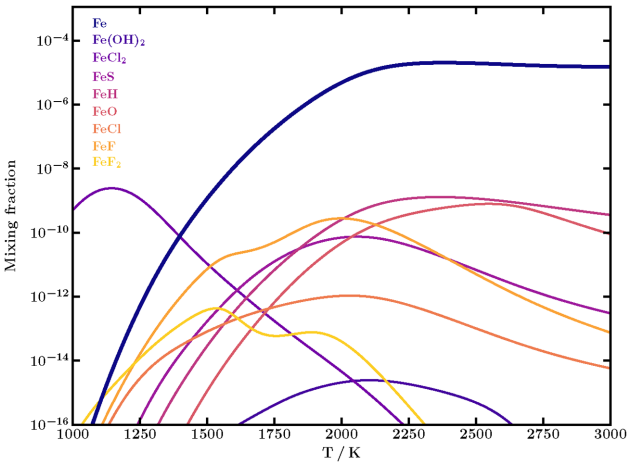

Figure 4. Equilibrium chemical abundances of several Fe-based neutral gaseous species at 1 mbar as a function of temperature. Abundances are calculated using the HSC CHEMISTRY software (version 8) assuming solar elemental abundances (Asplund et al. 2009). At the equilibrium temperature of WASP-121b (∼2400 K), neutral atomic Fe (bold line) is the dominant species.

4 RESULTS

4.1 Transmission spectrum of WASP-121b

We detect strong absorption from the atmosphere of WASP-121b through multiple features in the transmission spectrum. We measure the line contrast, denoted $\mathcal{D}$ as the amplitude of a Gaussian profile fit to the absorption feature. We use the `astropy` package, which performs a Levenberg–Marquardt Least-Squares fit. The H α line is detected with contrast $\mathcal{D} = 0.0187 \pm 0.0011$, centroid $\lambda_0 = 6562.93 \pm 0.02$ Å, and FWHM $= 0.75 \pm 0.05$ Å (Fig. 5). We confirm the previous detection of the Sodium doublet (Sindel 2018). We measure $\mathcal{D} = 0.0069 \pm 0.0012$, $\lambda_0 = 5890.01 \pm 0.06$ Å, and FWHM $= 0.73 \pm 0.09$ Å for the D2 line, and $\mathcal{D} = 0.0025 \pm 0.0009$,

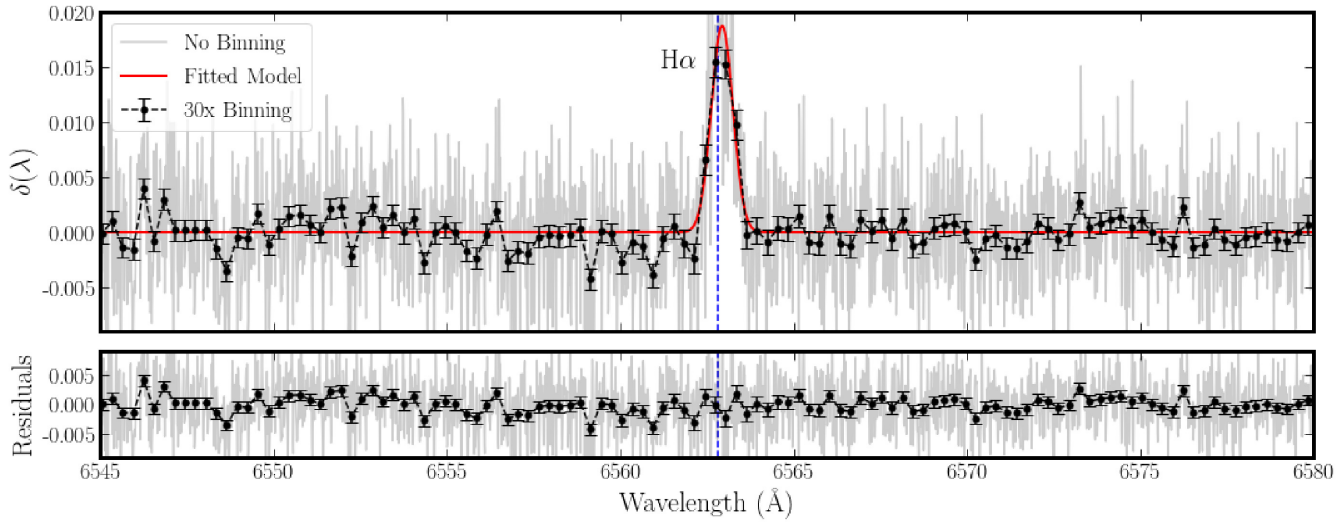

Figure 5. Excess transit depth from WASP-121b for the H α line. *Top panel*: combined data from all three nights of observation, stacked in the rest-frame of the planet. Also shown are the data binned 30×, and the best-fitting Gaussian profile to the absorption feature. *Bottom panel*: residuals in the data after subtracting the best-fitting profile. The expected centroid of H α is marked by a vertical blue line.

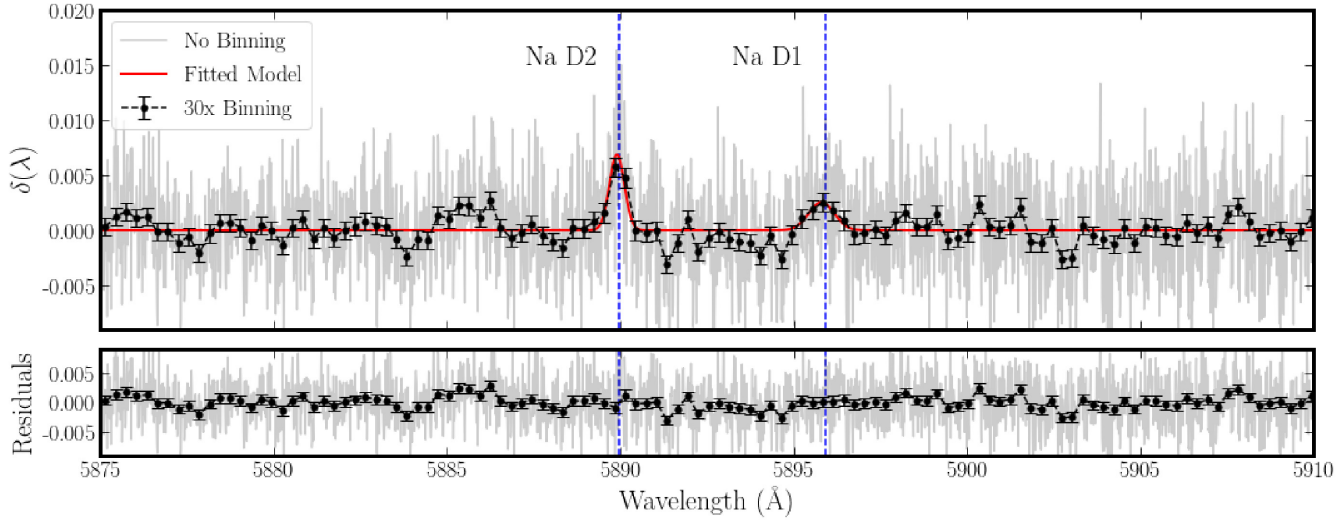

Figure 6. Same as Fig. 5, for the Sodium D lines. The expected centroids of the D1 and D2 features are marked by vertical blue lines.

$\lambda_0 = 5896.09 \pm 0.09$ Å, and FWHM $= 0.9 \pm 0.1$ Å for the D1 line (Fig. 6). These measurements are comparable with those reported in Sindel (2018). The transmission spectra shown in Figs 5 and 6 are in the rest-frame of the planet. The best-fitting centroids of the Na D lines are consistent with zero velocity offset. The H α line is offset by $+5.82 \pm 0.96$ km s^{-1}. We scan the transmission spectrum for signs of additional features. We find nominally excess absorption at 4340.75 , 4861.44, and 5169.02 Å (Fig. 7), which we attribute to H γ (4340.47 Å), H β (4861.33 Å), and Fe II (5169.03 Å) respectively. However, these features involve fewer data points and weaker line-contrasts. Hence we refrain from claiming definitive detections of these transitions.

In order to help rule out that our detections are from systematic or spurious artefacts, we perform the following control tests on the transmission spectrum: (1) randomization of in-transit and out-of-transit labels for individual exposures; (2) labelling even-numbered exposures as out-of-transit and odd-numbered exposures as in-transit; and (3) stacking the individual transmission spectra in the stellar rest frame. The resultant transmission spectra in the regions around the Na doublet and H α are shown in Fig. 8. Mixing in-transit and out-of-transit spectra eliminates the signal completely. The stellar rest-frame is dominated by RM artefacts, but also preserves some of the planetary signal. However, the features are weaker and less coherent.

We specify absorption depth as the ratio of two fluxes (Casasayas-Barris et al. 2017). The first is the mean flux of the stacked transmission spectrum $\hat{\mathfrak{R}}(\lambda)$, within a narrow pass-band centred on a feature; the second is the mean flux along the continuum, sampling points at longer and shorter wavelengths. We then subtract their ratio from unity. Pass-bands centred on the feature have sizes 0.188, 0.375, 0.75, 1.50, 3.0 Å. For the Na doublet, we select fluxes in the continuum spanning 5872.89–5884.89 Å and 5900.89–5912.89 Å. For H α, the continuum ranges are 6480.0–6492.0 Å and 6633.0–6645.0 Å. We additionally compute an Na doublet average by combining the fluxes sampled in both pass-bands. Our results are summarized in Table 3. The narrow pass-bands produce absorption depths comparable to the fitted line contrasts.

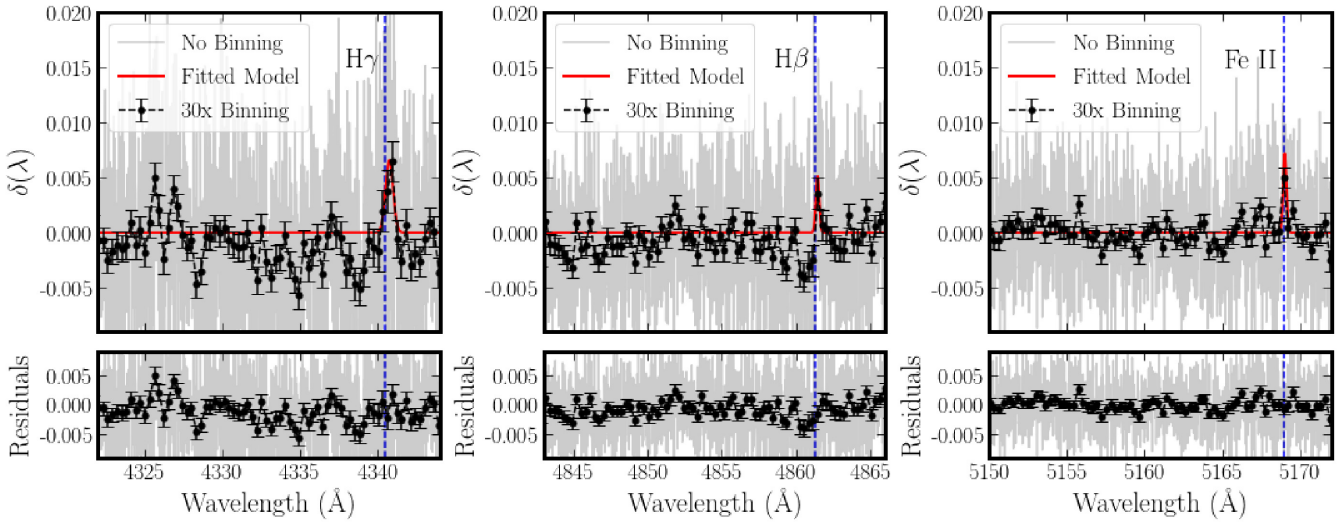

Figure 7. Same as Fig. 5, for three potential atmospheric absorption features, Hγ (left-hand panel), Hβ (middle), Fe II (right-hand panel). The expected centroids are marked by vertical blue lines.

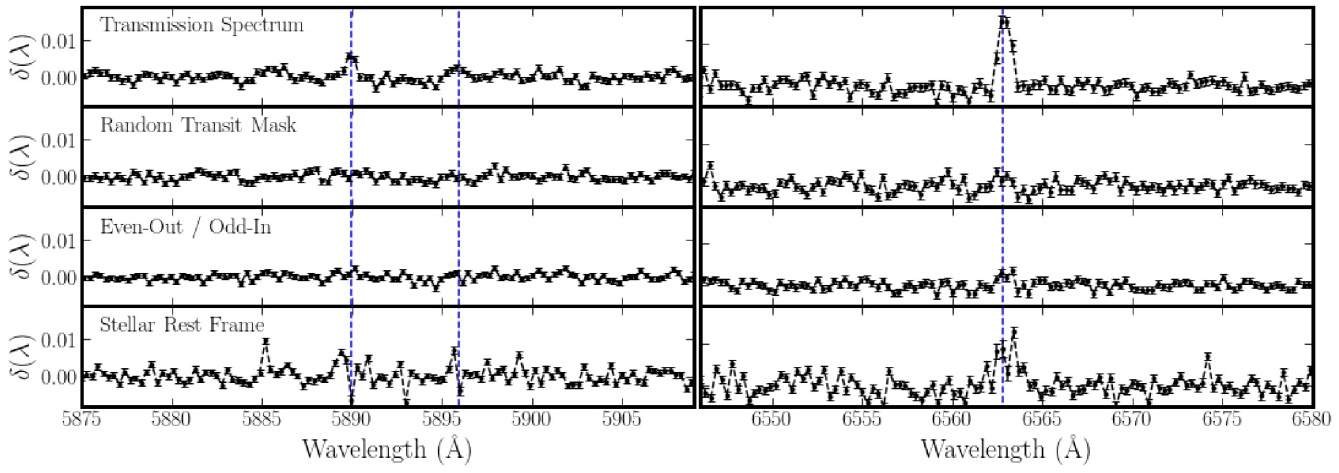

Figure 8. Excess transit depth from the atmosphere of WASP-121b, under different test calculations of the transmission spectrum, for regions surround the Na doublet (left-hand panel) and Hα (right-hand panel). *Top row*: the actual excess depth analysed in this study (no modifications); *Second row*: excess depth having randomized the in-transit and out-of-transit samples. *Third row*: excess depth with the out-of-transit sample composed of even frames, and the in-transit sample of odd frames. *Bottom row*: excess depth with the determined transit labels, but stacked in the rest-frame of the star instead of the planet.

Table 3. Summary of detections of Hα and the Sodium D lines. All values are given in percentages. Column 2: line contrast measured via fit of Gaussian profile to transmission absorption feature. Columns 3–7: absorption depths of features in the stacked transmission spectrum, for the labelled pass-bands. Columns 8–10: absorption depths of transmission light curves, measured via fit of a Gaussian profile, for the labelled pass-bands.

Feature	$\mathcal{D}$ [per cent]	$AD_{\Re}^{0.188Å}$	$AD_{\Re}^{0.375Å}$	$AD_{\Re}^{0.75Å}$	$AD_{\Re}^{1.5Å}$	$AD_{\Re}^{3.0Å}$	$AD_{LC}^{0.75Å}$	$AD_{LC}^{1.5Å}$	$AD_{LC}^{3.0Å}$
Hα	1.87 ± 0.11	1.80 ± 0.17	1.68 ± 0.12	1.38 ± 0.09	0.92 ± 0.06	0.39 ± 0.04	1.29 ± 0.17	0.97 ± 0.11	0.40 ± 0.06
Na D2	0.69 ± 0.12	0.89 ± 0.11	0.64 ± 0.08	0.49 ± 0.06	0.28 ± 0.04	0.10 ± 0.03	–	–	–
Na D1	0.25 ± 0.09	0.42 ± 0.11	0.26 ± 0.08	0.23 ± 0.06	0.18 ± 0.04	0.06 ± 0.03	–	–	–
Na Avg.	–	0.65 ± 0.08	0.45 ± 0.06	0.36 ± 0.04	0.23 ± 0.03	0.08 ± 0.02	0.46 ± 0.05	0.31 ± 0.04	0.18 ± 0.03

4.2 Light-curve analysis

We compute photometric transit light curves in a similar manner as Casasayas-Barris et al. (2019). We shift all transmission spectra $\Re(\lambda, t)$ to the planetary rest frame. For each spectrum, we determine the ratio of integrated line flux to integrated continuum flux, using the same 0.375, 0.75, 1.50 Å pass-bands and continuum ranges as in the previous section. There is a small phase interval around mid-transit where CLV and RM effects overlap with atmospheric absorption, manifesting as sharp spikes in the transmission light curve. We model CLV and RM contributions by simulating the transmission light curve of a planet without an atmosphere at the same phases as the data (Section 5.2). We then divide the observed light curve by the model, and fit the residuals using the `PyTransit` package (Parviainen 2015). We estimate limb-darkening

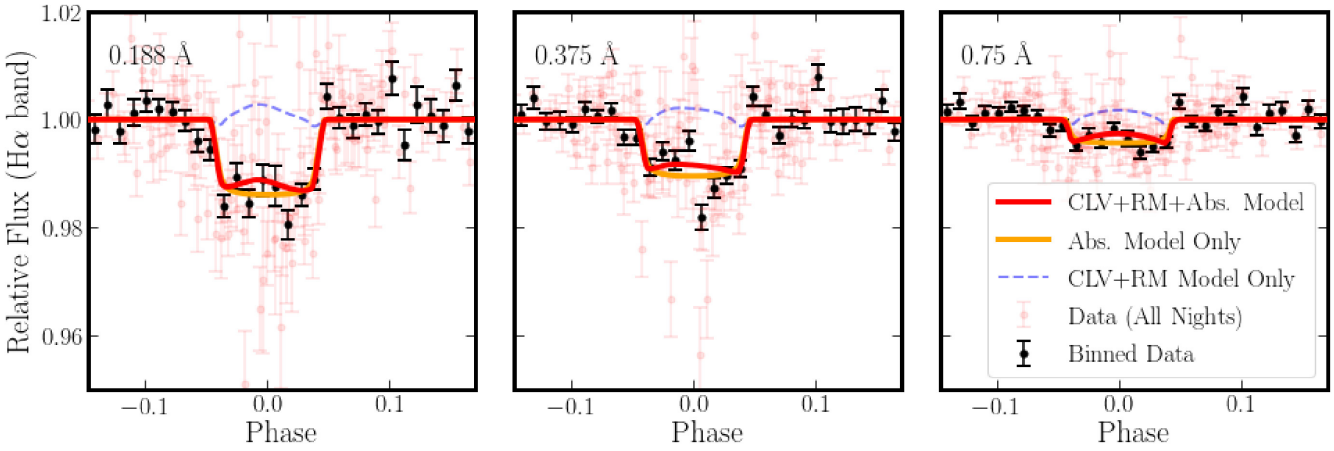

Figure 9. Transmission light curves for Hα for 0.375, 0.75, and 1.50 Å pass-bands. The blue dashed line depicts the theoretical contributions from centre-to-limb variation and the Rossiter–McLaughlin effect. The red line depicts the best-fitting absorption depth model, with included contributions from CLV and RM. Data from all nights were combined for the analysis.

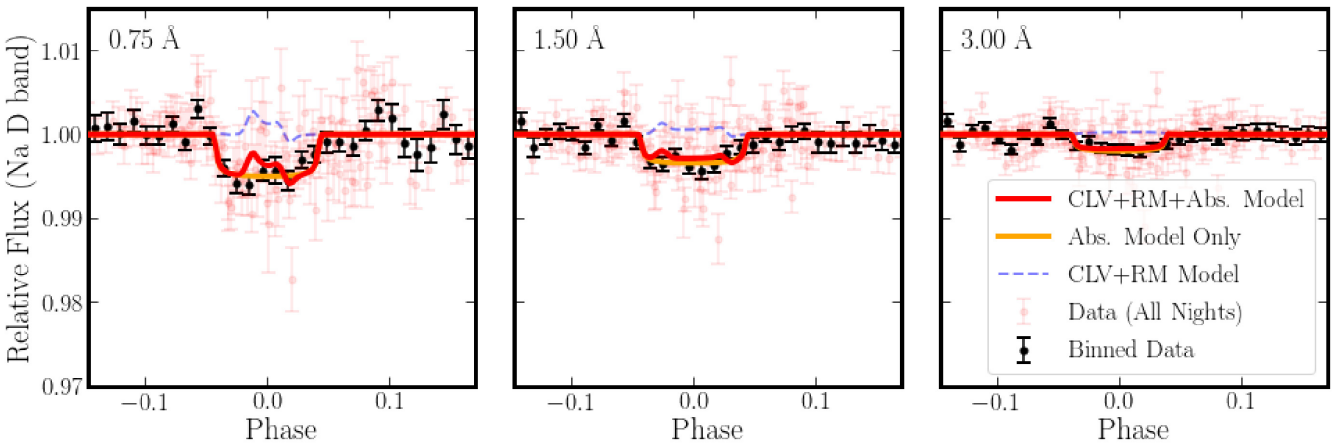

Figure 10. Same as Fig. 9, for the average depths of the Na D1 and Na D2 lines.

coefficients with the `LDTk` package (Parviainen & Aigrain 2015). The square of the fitted planet-to-star radii ratio is taken as an additional measurement of absorption depth. Light curves are shown in Figs 9 and 10 for Hα and the Na doublet average, respectively. Overall, the CLV+RM effect does not significantly impact the absorption depth measurement. The effect also averages out for the largest pass-bands. Minor differences between the observed and modelled CLV and RM effects may be attributed to our LTE assumption (Casasayas-Barris et al. 2018); also, we did not account for the effective radius of the planet R_λ, which is left as a free parameter in Casasayas-Barris et al. (2019). The absorption depths are listed in Table 3, and are consistent with the stacked transmission spectrum absorption depths.

4.3 Cross-correlation with atomic species

We detect neutral Fe at 5.3σ significance. The cross-correlation signal peaks at $K_p = 205^{+30}_{-29}$ and $RV = -3^{+3}_{-1}$ km s^{-1}, where uncertainties correspond to 1σ contours around the peak. Detection significance is defined as the number of standard deviations away from the mean in the entire sample of K_p–$V_{\rm sys}$ combinations (bottom panel, Fig. 11). The K_p–$V_{\rm sys}$ samples from Nights 1 and 3 have been averaged together. Our quoted significance is a conservative estimate, since we refrain from sampling $K_p < 100$ km s^{-1}. We reduced the noise in this region when we subtracted the Doppler Shadow model, and its inclusion would decrease the overall sample variance. We also avoided optimizing weights and masking during cross-correlation, which could lead to spurious signals (Cabot et al. 2019). Considering the cross-correlation function as a weighted average line depth in the species, we may approximate an equivalent transit depth to be 0.00082 ± 0.00014. We note this is well below the noise levels of the stacked transmission spectrum, which demonstrates the advantage of cross-correlation for species with many lines.

5 DISCUSSION

5.1 Implications for atmospheric structure

Based on line-contrasts, the Hα line probes $R \sim 1.51R_p$, and the Na D2 line probes $R \sim 1.20R_p$. Our ∼2 per cent Hα absorption depth suggests an extended Hydrogen atmosphere, possibly undergoing escape. Yan & Henning (2018) discuss a similar scenario for KELT-9b. The Hα line is significantly redshifted, by +5.82 ± 0.96 km s^{-1}. This is interesting in light of previous detections of blueshifted Hα features in UHJs. For example, high-altitude winds in MASCARA-2b were reported by Casasayas-Barris et al. (2019), who find a −3.0 to −4.5 km s^{-1}

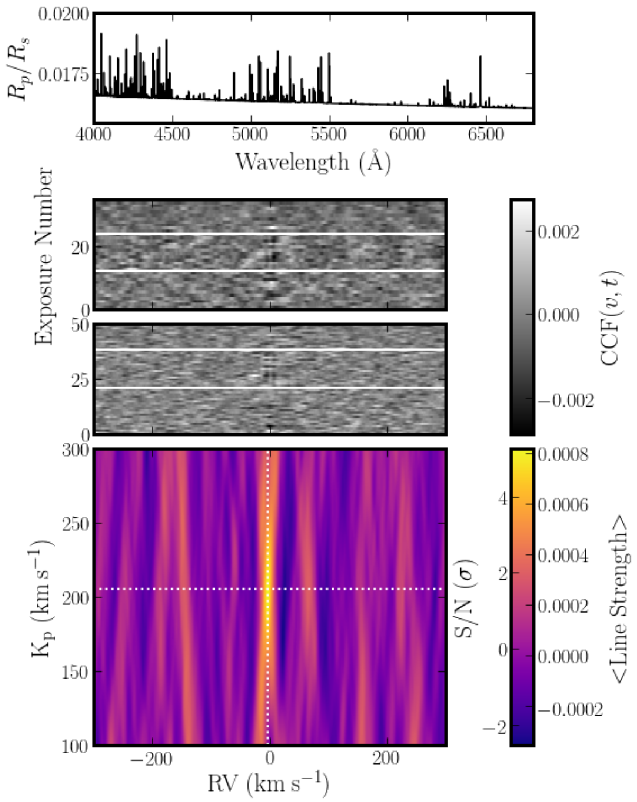

Figure 11. High-significance detection of Fe I via cross-correlation with a model template. *Top panel*: Plot of the Fe I model spectrum, which was baseline-subtracted and normalized to obtain the cross-correlation template. *Middle panel*: Time-series, residual cross-correlation functions (CCFs), which are obtained by subtracting the co-added out-of-transit CCF from all CCFs. The scaled Doppler shadow model has also been subtracted, leaving the planet signal as a faint, light trail. The horizontal white lines mark the start and end of transit. Spectra were Doppler shifted by the known V_{sys} of WASP-121 prior to cross-correlation. The two rows correspond to Nights 1 and 3. *Bottom panel*: Strength of the CCFs, co-added after being Doppler shifted by the velocity of WASP-121b. Different assumptions are made for K_p and V_{sys}, which in turn sample different possible velocities of the planet. The dotted white lines mark the location of the peak signal. The colour-map represents both detection significance, as well as the mean line-strength.

blueshifted Hα line. Our measurement may result from more complex gas motion in the exosphere, especially if the Hydrogen is undergoing escape. Another explanation may be planetary rotation, and differential chemistry between the morning and evening terminators. Motivated by the spatially resolved dynamics detected by Louden & Wheatley (2015), we recomputed the transmission spectrum using only ingress exposures as 'in-transit', and then using only egress exposures. The Hα absorption at ingress has a net 4.8 ± 2.6 km s^{-1} redshift, whereas at egress it is -0.5 ± 3.4 km s^{-1}. These uncertainties are large because of the smaller number of exposures in the ingress/egress compared to the full transit. A hydrodynamical model may be needed to precisely identify the origin of the redshift, which is beyond the scope of this study.

A nominal estimate based on the average line strength of Fe I, as discussed in §4.3, corresponds to $R \sim 1.03R_p$. These heights represent optical depths of $\tau \sim 0.56$ for a chord tracing the atmosphere annulus around the planet (Fortney 2005; Lecavelier Des Etangs et al. 2008; Howe & Burrows 2012). Fe I probably extends higher than $1.03R_p$, since single transitions may have deeper transit depths than the weighted-average depth.

The recovered average Fe I line strength is dependent on both the weighting scheme and model template used in cross-correlation. Nevertheless, the species hardly extends out to the radii of Fe II as measured by Sing et al. (2019), which reaches absorption depths of ∼10 per cent. The scatter of their *HST* STIS NUV transmission spectrum reaches $R \sim 1.4R_p$, which would prevent probing deep into the atmosphere. This explains why they only see one strong Fe I transition, corresponding to $R \sim 1.8R_p$, whereas their ion detections reach nearly $R \sim 3R_p$. Given the lower resolution at shorter wavelengths, cross-correlation may not be effective either. We note that Fe I opacity is strongest in the optical, and Fe II in the NUV. Hence, it follows that Fe is predominantly neutral at least out to $R \sim 1.03R_p$, and possibly out to $\sim 1.4R_p$.

Assuming $g = 843$ cm s^{-2} (derived from Table 2), $\mu = 2.22$ (mean molecular weight of Jupiter), and a nominal temperature of $T = T_{eq} = 2358$ K, WASP-121b has a pressure scale height $H_p = 1039$ km. Note, WASP-121b has a relatively large radius compared to other hot Jupiters, and is quite diffuse. Absorption out to one scale height produces an excess absorption depth of ∼240 ppm, comparable to the value quoted by Evans et al. (2018). Our Fe I absorption extends to $\sim 4H_p$, which corresponds to a pressure of $\sim 2 \times 10^{-3}$ bar assuming a typical $P_0 = 0.1$ bar corresponding to the white light radius (e.g. Welbanks & Madhusudhan 2019). The retrieved dayside Pressure-Temperature profile of WASP-121b exhibits a thermal inversion (Evans et al. 2017), where the temperature rises steeply between 10^{-2} and 10^{-4} bar. Despite the suggestions of a thermal inversion in WASP-121b being caused by H-, TiO, and/or VO, it is possible that Fe absorption may also contribute to the same. Our calculations of thermochemical equilibrium show that Fe can remain largely neutral as high up in the atmosphere as 10^{-6} bar for T ∼1500–3000 K, however photoionization is likely to contribute ionisation from Fe I to Fe II deeper in the atmosphere.

5.2 Centre-to-limb variation and Rossiter-McLaughlin effects

Ideally, dividing in-transit spectra by a co-added master out-of-transit spectrum isolates the atmospheric absorption. However, high-resolution spectroscopy resolves other differences between the out-of-transit spectrum and individual in-transit spectra. Centre-to-limb variation describes the change in specific-intensity as a function of distance from the centre of the star out to its limb (Yan et al. 2017), parametrized by the dimensionless quantity $1 \geq \mu \geq 0$. Absorption lines in spectra from the limb of the star probe cooler gas at optical depth $\tau = 1$. The continuum level also decreases from limb-darkening (Mandel & Agol 2002). Another important effect is from stellar rotation, which Doppler shifts light emanating further from the rotation axis. An out-of-transit spectrum averages these effects over the entire stellar disc. However, during a transit, the planet occults a region of the disc with its own local stellar line profile, affected by CLV and rotation. This distorts the average stellar spectrum, and produces a residual in the ratio of in-transit and out-of-transit spectra (the distortion is called the Rossiter–McLaughlin effect, only considering stellar rotation). The residual can create spurious features in the transmission spectrum and photometric light curves of individual lines (Louden & Wheatley 2015; Yan et al. 2015, 2017; Casasayas-Barris et al. 2018, 2019).

In order to evaluate the influence of CLV and RM effects in the observed data, we model them simultaneously in a manner similar to Casasayas-Barris et al. (2019). We generate a synthetic spectrum of WASP-121 at 21 μ-angles with `Spectroscopy Made Easy`

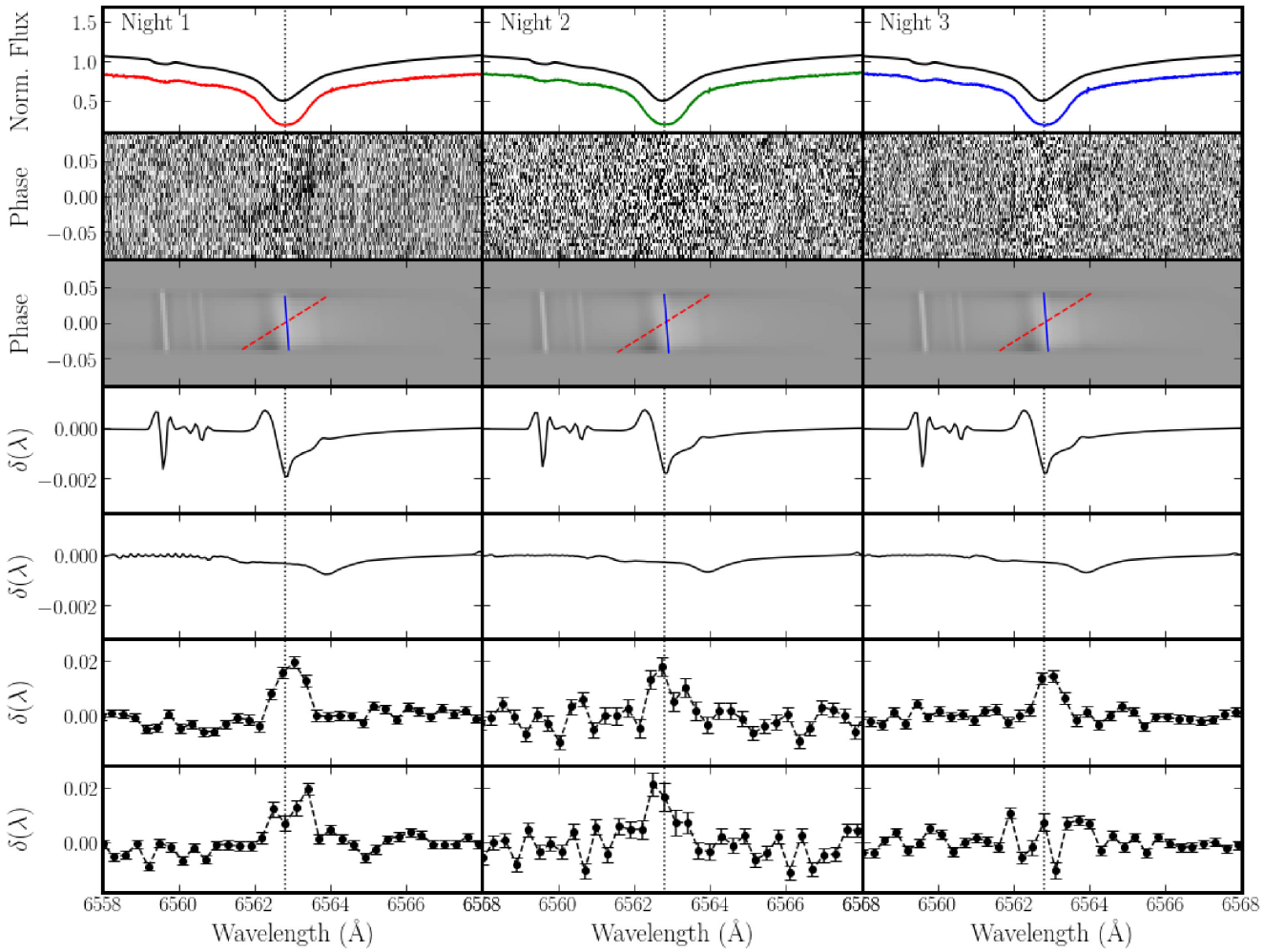

Figure 12. Comparison between the observed transmission spectra, and theoretical models of the CLV and RM effects, in the Hα region. Each column represents a different night of observation. *Top row*: the stacked and normalized out-of-transit stellar spectrum (coloured line) and the integrated model stellar line profile (black line). *Second row*: time-series transmission spectra for each night. The colour range is from −0.05 (black) to 0.05 (white). Planetary atmosphere absorption is particularly visible in data from Nights 1 and 3. *Third row*: modelled time-series transmission spectra, assuming the parameters in Table 2 and no atmosphere. The colour range is from −0.01 (black) to 0.01 (white). The blue solid line denotes the position of Hα, Doppler shifted by the velocity of the occulted stellar region (RM effect). The red dashed line denotes the position of Hα, Doppler shifted by the expected planet velocity. *Fourth row*: the jointly modelled CLV+RM effects, summed in the stellar rest-frame. *Fifth row*: the jointly modelled CLV+RM effects, summed in the planetary rest-frame. *Sixth row*: Transmission spectra summed in the planetary rest-frame. Note the change in y-axis scale. *Seventh row*: Transmission spectra summed in the stellar rest-frame. The vertical dotted lines marked the rest-frame wavelength of Hα.

(SME) (Valenti & Piskunov 1996), using the VALD3 line-list data base (Ryabchikova et al. 2015) and Kurucz ATLAS9 solar atmosphere models, and assuming parameters of $T_{\rm eff} = 6460$ K, $\log g = 4.2$ and [Fe/H] = 0.13. We do not investigate non-LTE effects, or dependence of individual features on [Fe/H]. The stellar disc is simulated on an 80 × 80 pixel grid. Each pixel is allocated a spectrum, linearly interpolated between computed μ values, and Doppler shifted by the local rotation speed of the star. We assume $\lambda = -257.8^\circ$ and $v \sin i = 13.56\,{\rm km\,s^{-1}}$. We integrate the flux from each pixel over the full disc to obtain an out-of-transit spectrum. We model the transit according to the prescription of Cegla et al. (2016), treating the planet as an opaque disc with no atmosphere. The planet's projected position on the stellar disc is given by,

$$x_p = \frac{a}{R_*} \sin 2\pi\phi \tag{10}$$

$$y_p = -\frac{a}{R_*} \cos 2\pi\phi \cos i_p. \tag{11}$$

After rotating by the sky-projected obliquity, the position becomes,

$$x_\perp = x_p \cos\lambda - y_p \sin\lambda \tag{12}$$

$$y_\perp = x_p \sin\lambda + y_p \cos\lambda \tag{13}$$

and the planet occults a portion of the stellar disc with radial velocity,

$$v_{\rm RM} = x_\perp v \sin i. \tag{14}$$

The CLV is determined by the cosine of the angle (θ) between the stellar normal and the observer,

$$\mu = \cos\theta = (1 - (r_p/R_*)^2)^{1/2}, \tag{15}$$

where $r_p^2 = x_p^2 + y_p^2$ (Mandel & Agol 2002). For each night, at each phase, we compute in-transit spectra by integrating over all pixels obscured by the planet, and subtracting the result from the out-of-transit spectrum. We then divide by the out-of-transit spectrum,

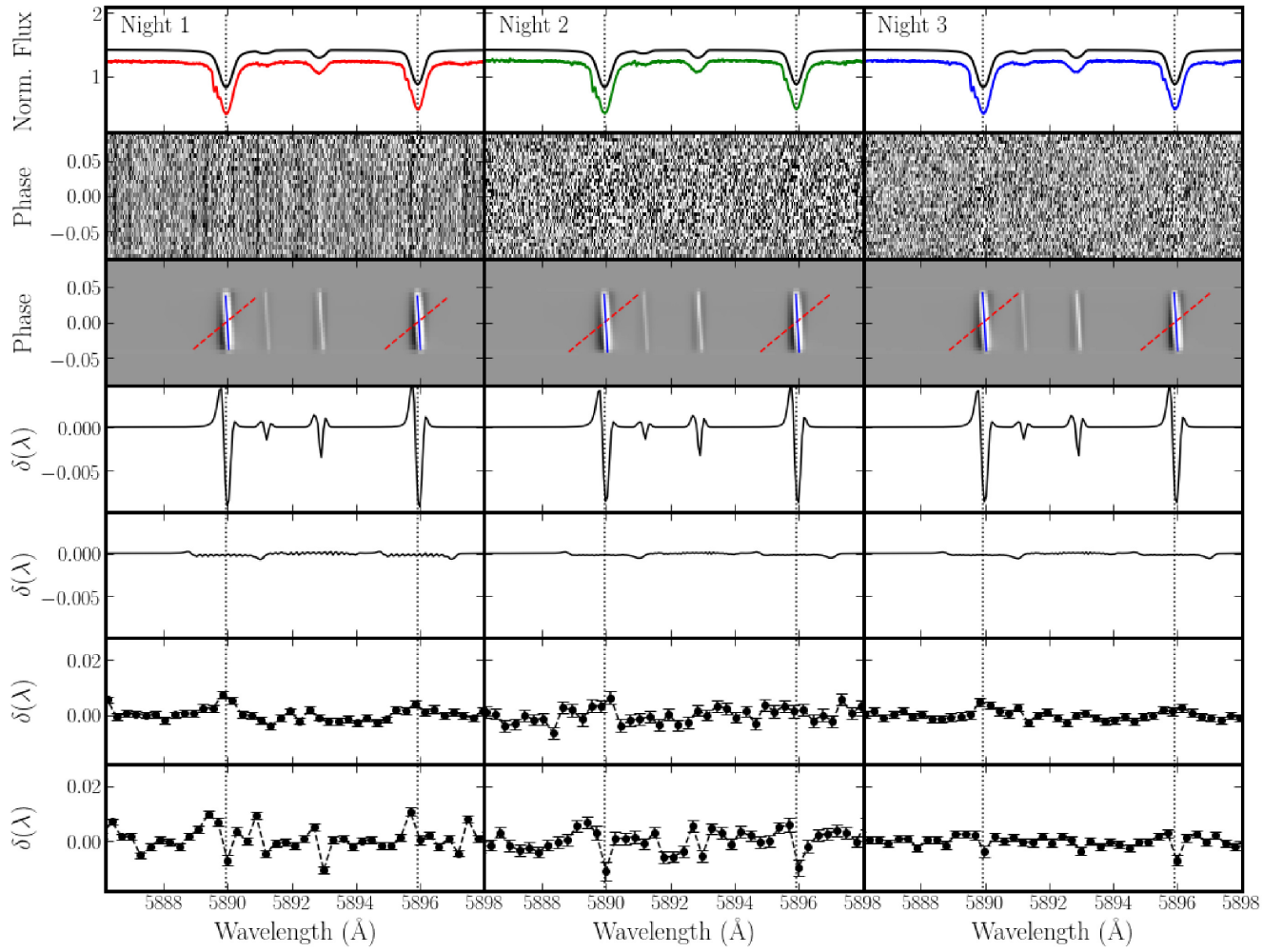

Figure 13. Same as Fig. 12, except for the Sodium D lines.

normalize the continuum by a low-order polynomial, and subtract unity. For computational reasons, we narrow the wavelength range, around H α at first. We stack the transmission spectra in the rest frames of the planet and star. This model is shown in Fig. 12, along with the corresponding data. We repeat the analysis for the Na doublet region (Fig. 13). The planet rest-frame residual is at the 0.073 per cent level for H α and the 0.057 per cent level for Na lines, which are negligible compared to the measured line strengths of 1.87 per cent for H α and 0.25–0.69 per cent for Na. Further, they are less than the 1σ uncertainties on the line depths, of 0.11 per cent for H α and 0.09–0.12 per cent for Na. If we increase the nominal radius of the planet by 1.5×, then the residuals are at a 0.16 per cent level for H α and 0.12 per cent. While these are comparable to the uncertainties, the deepest parts of the residuals lie ∼1.5 Å redshifted from the line centroids, which further increases our confidence that the CLV and RM effects do not affect our absorption measurements. The stellar rest-frame residuals are about 3 × larger for H α, and 15 × larger for the Na lines. In the third row of Fig. 12, we show the expected positions of H α features from planetary absorption (red-dashed line, corresponding to $v = v_{\rm pl}$) and the RM effect (blue-solid line, corresponding to $v = v_{\rm RM}$). Since the orbit of WASP-121b is polar, these two trails are highly non-parallel. Hence, stacking in the planet frame (red-dashed line) smears out the already small RM effect (fifth row of Fig. 12). However, stacking in the stellar frame produces a large artefact, since the RM trail is nearly vertical (fourth row of Fig. 12). Note that the stellar rest-frame residuals are similar in shape and amplitude to the observed ones (fourth row, Fig. 8), and the RM artefacts exhibit the negative-winged shape described in the previous section.

When do RM and CLV effects become significant in transmission spectroscopy? Yan et al. (2017) thoroughly explore CLV, finding that low $T_{\rm eff}$ hosts exhibit stronger CLV artefacts. They also show the dependence on impact parameter (b). For the RM effect, one must also consider the sky projected obliquity (λ). We perform a systematic investigation of joint contributions of CLV and RM to transmission spectra for various orbits around WASP-121. As above, we model the planet as an opaque disc without an atmosphere in the following orbits: (1) the identical orbit as WASP-121b, as modelled above; (2) an aligned orbit with $\lambda = 0.0$; (3) an exactly polar orbit of $\lambda = -270.0$; (4) an edge-on orbit with $b = 0.0$; (5) an inclined orbit expected to maximize the CLV effect, $b = b_{\rm max} = 0.84$ (Yan et al. 2017). Transmission spectra are calculated at 50 equally spaced phases $-0.06 < \phi < 0.06$, and subsequently stacked in seven different rest-frames. These include the stellar rest-frame and the planet rest-frame under different assumptions of semi-amplitude (K_p). We additionally define an 'RM-frame', which is Doppler shifted by the velocity of the occulted region of the stellar disc ($v_{\rm RM}$) (equation 14). We note that explicit exclusion of

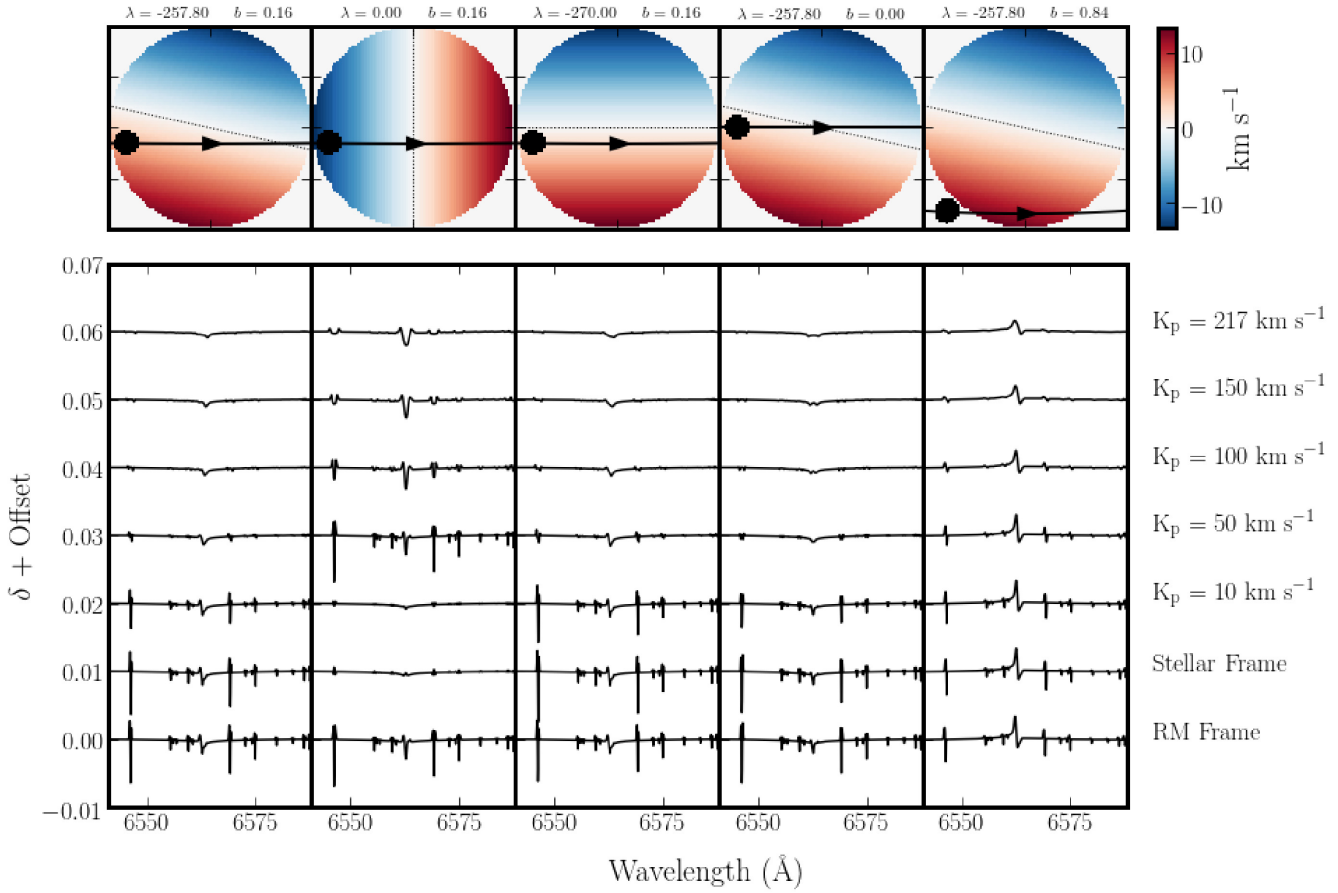

Figure 14. Theoretical contributions to transmission spectra from the jointly modelled centre-to-limb variation and Rossiter-McLaughlin effects. We assume a star with effective temperature and radius of WASP-121, and a planet with the radius and semimajor axis of WASP-121b. *Top row*: planetary orbits explored for different choices of projected obliquity and impact parameter (the left-most column represents the actual orbit of WASP-121b). The transmission spectra are stacked in seven different rest frames including: the velocites of the occulted stellar regions (RM Frame); zero-velocity (the Stellar Frame); and different assumptions of the planetary semi-amplitude, including the physical value for WASP-121b of 217 km s^{-1}. The analysis is restricted to the region around Hα.

ingress and egress spectra did not change results appreciably. All results are predominantly from the RM effect. This was tested by running the simulations with $v \sin i = 0.0\,\mathrm{km\,s^{-1}}$, which produced much smaller CLV-only artefacts. We did not explore dependence on the planet radius. A larger radius should exacerbate the effects (Di Gloria, Snellen & Albrecht 2015).

Our results are shown in Fig. 14. In nearly all cases, a growing K_p increasingly smears out the artefacts. Setting $K_p = 10\,\mathrm{km\,s^{-1}}$ corresponds to a slow, distant orbit, while $K_p = 217\,\mathrm{km\,s^{-1}}$ is the fast, close-in orbit of WASP-121b. The polar and near-polar orbits produce strong residuals in the stellar rest frame. As expected for an aligned orbit (second column), the RM effect approximately cancels out in the stellar rest frame, but is strong in the planet rest frame (Louden & Wheatley 2015). In this case, it is notable that the artefacts spike at $K_p = 50\,\mathrm{km\,s^{-1}}$. This is because the planet and RM velocities are very similar (the trails are nearly parallel). As such, stacking in the planet frame is nearly equivalent to perfectly summing the RM artefact in its own frame (bottom row). This is an important consideration for observations of long-period planets. For a circular and edge-on orbit, one can estimate $K_p \simeq 2\pi a/P$, ingress and egress phases as $\phi_{\mathrm{out}} \simeq -\phi_{\mathrm{in}} \simeq R_*/2\pi a$, with $\Delta v_p = K_p(\sin 2\pi\phi_{\mathrm{out}} - \sin 2\pi\phi_{\mathrm{in}})$, and $\Delta v_{\mathrm{RM}} = v_{\mathrm{RM}}(\phi_{\mathrm{out}}) - v_{\mathrm{RM}}(\phi_{\mathrm{in}})$ (which equals $v \sin i(\sin 2\pi\phi_{\mathrm{out}} - \sin 2\pi\phi_{\mathrm{in}})$ for an aligned orbit). RM artefacts are maximized when $\Delta v_p \sim \Delta v_{\mathrm{RM}}$.

6 CONCLUSION

The ultra-hot Jupiter WASP-121b exhibits some of the most extreme and fascinating properties amongst giant exoplanets, including a particularly close-in orbit and high equilibrium temperature. It represents a corner case in planetary formation theory based on its orbital properties, and an important atmospheric case study for its thermal inversion (Evans et al. 2017) and extended atmosphere (Sing et al. 2019). In this study, we have presented a detailed analysis of the optical transmission spectrum of WASP-121b at high-resolution. We resolve nearly 2 per cent excess atmospheric absorption from Hα, and 0.5–1 per cent absorption from the Sodium D lines. The Hα detection supports an extended and possibly escaping atmosphere. We present the additional high-significance detection of neutral Fe via the cross-correlation method (Snellen et al. 2010). While it is difficult to determine the exact extent of the region in the atmosphere containing Fe I, we find it lies approximately within stratosphere, possibly linking it to the thermal inversion. We additionally present a detailed analysis of the Rossiter-McLaughlin effect and centre-to-limb variation, and how they impact the observed transmission spectra.

Our characterization of WASP-121b comes at a time of systematic investigation of exoplanet atmospheres. Not only are multiple molecular and atomic detections being made in individual planets,

but it is becoming possible to start comparing the chemical abundances of different planets (Madhusudhan 2019). The detections of H, Na, and Fe presented here add to a constantly growing list of detections in different wavelength regimes and at different spectral resolutions. Current and forthcoming generations of high-resolution optical spectrographs, including HARPS, HARPS-N, and the recently commissioned ESPRESSO (Pepe et al. 2013) and EXPRES (Jurgenson et al. 2016), offer great potential for such studies, in pursuit of characterizing new planets, and in search of new and insightful chemistry.

ACKNOWLEDGEMENTS

LW acknowledges support from the Gates Cambridge Trust towards his doctoral research. AP acknowledges support from STFC towards her doctoral research. SG acknowledges support from the UK Science and Technology Facilities Council (STFC) research grant ST/S000631/1.

REFERENCES

Allart R., Lovis C., Pino L., Wyttenbach A., Ehrenreich D., Pepe F., 2017, A&A, 606, A144
Alonso-Floriano F. J. et al., 2019, A&A, 621, A74
Anderson D. R. et al., 2018, preprint (arXiv:1809.04897)
Arcangeli J. et al., 2018, ApJ, 855, L30
Asplund M., Grevesse N., Sauval A. J., Scott P., 2009, ARA&A, 47, 481
Batygin K., Bodenheimer P. H., Laughlin G. P., 2016, ApJ, 829, 114
Birkby J. L., 2018, Spectroscopic Direct Detection of Exoplanets. Springer International Publishing, Cham, p. 1485
Birkby J. L., de Kok R. J., Brogi M., de Mooij E. J. W., Schwarz H., Albrecht S., Snellen I. A. G., 2013, MNRAS, 436, L35
Birkby J. L., de Kok R. J., Brogi M., Schwarz H., Snellen I. A. G., 2017, AJ, 153, 138
Bond J. C., Lauretta D. S., O'Brien D. P., 2010, Icarus, 205, 321
Bourrier V. et al., 2019, preprint (arXiv:1909.03010)
Brogi M., Snellen I. A. G., de Kok R. J., Albrecht S., Birkby J., de Mooij E. J. W., 2012, Nature, 486, 502
Brogi M., de Kok R. J., Albrecht S., Snellen I. A. G., Birkby J. L., Schwarz H., 2016, ApJ, 817, 106
Brogi M., Giacobbe P., Guilluy G., de Kok R. J., Sozzetti A., Mancini L., Bonomo A. S., 2018, A&A, 615, A16
Cabot S. H. C., Madhusudhan N., Hawker G. A., Gandhi S., 2019, MNRAS, 482, 4422
Cartier K. M. S. et al., 2017, AJ, 153, 34
Casasayas-Barris N., Palle E., Nowak G., Yan F., Nortmann L., Murgas F., 2017, A&A, 608, A135
Casasayas-Barris N. et al., 2018, A&A, 616, A151
Casasayas-Barris N. et al., 2019, A&A, 628, A9
Cauley P. W., Shkolnik E. L., Ilyin I., Strassmeier K. G., Redfield S., Jensen A., 2019, AJ, 157, 69
Cegla H. M., Lovis C., Bourrier V., Beeck B., Watson C. A., Pepe F., 2016, A&A, 588, A127
Dawson R. I., Johnson J. A., 2018, ARA&A, 56, 175
Daylan T. et al., 2019, preprint (arXiv:1909.03000)
Delrez L. et al., 2016, MNRAS, 458, 4025
Di Gloria E., Snellen I. A. G., Albrecht S., 2015, A&A, 580, A84
Ehrenreich D. et al., 2015, Nature, 522, 459
Elser S., Meyer M. R., Moore B., 2012, Icarus, 221, 859
Espinoza N. et al., 2019, MNRAS, 482, 2065
Evans T. M. et al., 2016, ApJ, 822, L4
Evans T. M. et al., 2017, Nature, 548, 58
Evans T. M. et al., 2018, AJ, 156, 283
Ford E. B., Rasio F. A., 2006, ApJ, 638, L45
Fortney J. J., 2005, MNRAS, 364, 649
Fortney J. J., Lodders K., Marley M. S., Freedman R. S., 2008, ApJ, 678, 1419
Gandhi S., Madhusudhan N., 2017, MNRAS, 472, 2334
Gandhi S., Madhusudhan N., 2019, MNRAS, 485, 5817
Gandhi S., Madhusudhan N., Hawker G., Piette A., 2019, ApJ, 158, 228
Harrison J. H. D., Bonsor A., Madhusudhan N., 2018, MNRAS, 479, 3814
Hawker G. A., Madhusudhan N., Cabot S. H. C., Gandhi S., 2018, ApJ, 863, L11
Hoeijmakers H. J. et al., 2018, Nature, 560, 453
Hoeijmakers H. J. et al., 2019, A&A, 627, A165
Howe A. R., Burrows A. S., 2012, ApJ, 756, 176
Husser T.-O., Wende-von Berg S., Dreizler S., Homeier D., Reiners A., Barman T., Hauschildt P. H., 2013, A&A, 553, A6
Jurgenson C., Fischer D., McCracken T., Sawyer D., Szymkowiak A., Davis A., Muller G., Santoro F., 2016, in Proc. SPIE Conf. Ser. Vol. 9908, EXPRES: a next generation RV spectrograph in the search for earth-like worlds. SPIE, Bellingham, p. 99086T
Kitzmann D. et al., 2018, ApJ, 863, 183
Kramida A., Ralchenko Y., Reader J., NIST ASD Team, 2018, NIST Atomic Spectra Database (ver. 5.6.1), [Online]. National Institute of Standards and Technology, Gaithersburg, MD. Available at: https://physics.nist.gov/asd [2019, February 6]
Lecavelier Des Etangs A., Pont F., Vidal-Madjar A., Sing D., 2008, A&A, 481, L83
Lockwood A. C., Johnson J. A., Bender C. F., Carr J. S., Barman T., Richert A. J. W., Blake G. A., 2014, ApJ, 783, L29
Lothringer J. D., Barman T., Koskinen T., 2018, ApJ, 866, 27
Louden T., Wheatley P. J., 2015, ApJ, 814, L24
Madhusudhan N., 2012, ApJ, 758, 36
Madhusudhan N., 2019, ARA&A, 57, 617
Madhusudhan N., Knutson H., Fortney J. J., Barman T., 2014a, in Beuther H., Klessen R. S., Dullemond C. P., Henning T., eds, Protostars and Planets VI. University of Arizona Press, Tucson, AZ, p. 739
Madhusudhan N., Amin M. A., Kennedy G. M., 2014b, ApJ, 794, L12
Mandel K., Agol E., 2002, ApJ, 580, L171
Mikal-Evans T. et al., 2019, MNRAS, 488, 2222
Mollière P., van Boekel R., Dullemond C., Henning T., Mordasini C., 2015, ApJ, 813, 47
Moriarty J., Madhusudhan N., Fischer D., 2014, ApJ, 787, 81
Nortmann L. et al., 2018, Science, 362, 1388
Nugroho S. K., Kawahara H., Masuda K., Hirano T., Kotani T., Tajitsu A., 2017, AJ, 154, 221
Öberg K. I., Murray-Clay R., Bergin E. A., 2011, ApJ, 743, L16
Parmentier V. et al., 2018, A&A, 617, A110
Parviainen H., 2015, MNRAS, 450, 3233
Parviainen H., Aigrain S., 2015, MNRAS, 453, 3821
Pasek M. A., Milsom J. A., Ciesla F. J., Lauretta D. S., Sharp C. M., Lunine J. I., 2005, Icarus, 175, 1
Pepe F. et al., 2013, Messenger, 153, 6
Pinhas A., Rackham B. V., Madhusudhan N., Apai D., 2018, MNRAS, 480, 5314
Piskorz D. et al., 2016, ApJ, 832, 131
Richard C. et al., 2012, J. Quant. Spec. Radiat. Transf., 113, 1276
Rodler F., Kürster M., Barnes J. R., 2013, MNRAS, 432, 1980
Ryabchikova T., Piskunov N., Kurucz R. L., Stempels H. C., Heiter U., Pakhomov Y., Barklem P. S., 2015, Phys. Scr., 90, 054005
Salz M., Schneider P. C., Fossati L., Czesla S., France K., Schmitt J. H. M. M., 2019, A&A, 623, A57
Seidel J. V. et al., 2019, A&A, 623, A166
Sheppard K. B., Mandell A. M., Tamburo P., Gand hi S., Pinhas A., Madhusudhan N., Deming D., 2017, ApJ, 850, L32
Sindel J. P., 2018, Masters dissertation, Luleå University
Sing D. K. et al., 2019, AJ, 158, 91
Smette A. et al., 2015, A&A, 576, A77

Snellen I. A. G., de Kok R. J., de Mooij E. J. W., Albrecht S., 2010, Nature, 465, 1049
Tamuz O., Mazeh T., Zucker S., 2005, MNRAS, 356, 1466
Triaud A. H. M. J. et al., 2010, A&A, 524, A25
Valenti J. A., Piskunov N., 1996, A&AS, 118, 595
Welbanks L., Madhusudhan N., 2019, AJ, 157, 206
Wyttenbach A., Ehrenreich D., Lovis C., Udry S., Pepe F., 2015, A&A, 577, A62
Yan F., Henning T., 2018, Nat. Astron., 2, 714
Yan F., Fosbury R. A. E., Petr-Gotzens M. G., Zhao G., Pallé E., 2015, A&A, 574, A94
Yan F., Pallé E., Fosbury R. A. E., Petr-Gotzens M. G., Henning T., 2017, A&A, 603, A73

This paper has been typeset from a TEX/LATEX file prepared by the author.